



ARTICLE

<https://doi.org/10.1038/s41467-019-10524-2>

OPEN

Polymorph selection towards photocatalytic gaseous CO₂ hydrogenation

Tingjiang Yan^{1,2,4}, Lu Wang^{2,4}, Yan Liang³, Meysam Makaremi ², Thomas E. Wood², Ying Dai³, Baibiao Huang³, Feysal M. Ali², Yuchan Dong² & Geoffrey A. Ozin ²

Titanium dioxide is the only known material that can enable gas-phase CO₂ photocatalysis in its anatase and rutile polymorphic forms. Materials engineering of polymorphism provides a useful strategy for optimizing the performance metrics of a photocatalyst. In this paper, it is shown that the less well known rhombohedral polymorph of indium sesquioxide, like its well-documented cubic polymorph, is a CO₂ hydrogenation photocatalyst for the production of CH₃OH and CO. Significantly, the rhombohedral polymorph exhibits higher activity, superior stability and improved selectivity towards CH₃OH over CO. These gains in catalyst performance originate in the enhanced acidity and basicity of surface frustrated Lewis pairs in the rhombohedral form.

¹The Key Laboratory of Life-Organic Analysis, College of Chemistry and Chemical Engineering, Qufu Normal University, Qufu, Shandong 273165, P. R. China.

²Materials Chemistry and Nanochemistry Research Group, Solar Fuels Cluster, Department of Chemistry, University of Toronto, 80 St. George Street, Toronto, ON M5S 3H6, Canada. ³School of Physics, State Key Laboratory of Crystal Materials, Shandong University, Jinan, Shandong 250100, P. R. China. ⁴These authors contributed equally: Tingjiang Yan and Lu Wang. Correspondence and requests for materials should be addressed to T.Y. (email: tingjiangn@163.com) or to Y.D. (email: daiy60@sdu.edu.cn) or to G.A.O. (email: gozin@chem.utoronto.ca)

A breakthrough in CO₂ photocatalysis often begins with materials discovery, and then, the challenges of optimizing its performance metrics by materials engineering follows. Through human intelligence and experiential learning, complemented by artificial intelligence and machine learning, one can hone the chemical and physical properties of a material to achieve the desired catalyst optimization for a targeted technology.

In the case of gas-phase heterogeneous hydrogenation of CO₂ to chemicals and fuels, performance optimization usually involves fine tuning the chemical and physical properties of the (photo) catalyst^{1–3}. This can be achieved by doping^{4,5}, isomorphous and aliovalent substitution^{6,7}, size control^{8,9}, morphology changes^{10,11}, heterostructuring^{12–14}, and support and promoter effects^{15–17}.

In this endeavor, a strategy rarely employed in catalyst optimization is polymorph selection, whereby the crystal structure of the catalyst material is changed, whereas its composition is retained. The challenge today is moving beyond titanium dioxide anatase and rutile polymorphs and discovering other compositions that exhibit polymorphism and enable CO₂ (photo)catalysis.

Indium-based semiconductor materials have been reported as promising photocatalysts in terms of their geometric structures and electronic configurations, which can possibly enhance the mobility and separation efficiency of charge carriers and improve photocatalytic activity^{18,19}. Numerous attempts have been made in recent years to develop various indium-based photocatalysts, such as oxides or mixed oxides^{20,21}, binary and ternary sulfides^{22,23}, hydroxides and oxyhydroxides^{24,25}, In-MOF²⁶, and so on. Among them, indium oxide (In₂O₃) is an n-type semiconductor with mainly two polymorphic phases, cubic and metastable rhombohedral phases²⁷. Pan et al.²⁸ and co-workers have demonstrated that cubic In₂O₃ nanobelts coated by carbon layer showed highly enhanced photocatalytic reduction of CO₂ to CO and CH₄ in aqueous solution with Pt as co-catalyst. Our group has reported that the cubic indium oxide nanocrystals with surface defects in the form of oxygen vacancies and hydroxyl groups, denoted as In₂O_{3-x}(OH)_y, can be utilized as an active catalyst towards photocatalytic gaseous CO₂ hydrogenation owing to advantageous surface, optical, and electronic properties²⁹. The CO₂ hydrogenation performance of the cubic In₂O_{3-x}(OH)_y polymorph can be further boosted by assembling nanocrystals into rod-like superstructures, which gives rise to an improved conversion rate for the reverse water gas shift reaction and a champion rate for solar methanol production at atmospheric pressure^{10,30}.

Herein, we have discovered that the rhombohedral form of indium oxide, like its cubic polymorph, is a highly active and selective heterogeneous (photo)catalyst for hydrogenating gaseous CO₂ to CO and CH₃OH. Significantly, the rhombohedral polymorph outperforms the cubic polymorph in terms of its catalytic activity, long-term stability, and selectivity towards CH₃OH. These performance enhancements stem from an increase in the acidity and basicity of surface frustrated Lewis pairs (SFLP) in the rhombohedral compared with the cubic polymorph.

Results

Synthesis and structural characterizations of rhombohedral In₂O_{3-x}(OH)_y. The rhombohedral In₂O_{3-x}(OH)_y nanocrystals (annealing at 350 °C and denoted as rh-In₂O_{3-x}(OH)_y) were synthesized via a thermal dehydration of an InOOH precursor, which was initially synthesized from a simple solvothermal system³¹. The obtained InOOH precursor is composed of monodispersed nanoparticles with the size of ~20 nm (Supplementary Fig. 1).

After thermal treatment at 350 °C, the resultant rh-In₂O_{3-x}(OH)_y nanocrystals maintained a similar particle size and exhibited a walnut shell-like morphology, which contained considerable nanopores in each nanocrystal (Fig. 1a). Such unique morphology could be caused by the loss of water from the lattice of the InOOH nanocrystal, which was confirmed by thermogravimetry (TG) and derivative thermogravimetry (DTG) analysis (Supplementary Fig. 2). In this case, the presence of these nanopores did not contribute much to the specific surface area of rh-In₂O_{3-x}(OH)_y. As a result, the as-prepared rh-In₂O_{3-x}(OH)_y has a specific surface area of 56 m² g⁻¹ and a pore size of 11 nm (Supplementary Fig. 3). The high-resolution transmission electron microscopy (HRTEM) images (Fig. 1b and Supplementary Fig. 4) indicate well-defined lattice fringes with inter-planar distances of 0.274 nm and 0.288 nm, which correspond to the (110) and (104) facets of rhombohedral In₂O₃, respectively. The powder X-ray diffraction (PXRD) patterns confirm that the precursor is orthorhombic InOOH, and leads to the formation of the corundum structure type of In₂O₃ (Fig. 1c). An obvious shift in binding energy was observed from the high-resolution X-ray photoelectron spectroscopy (XPS) of In 3d core level spectra for samples before and after annealing, indicating the conversion from InOOH to In₂O_{3-x}(OH)_y (Supplementary Fig. 5). The O 1s core level XPS spectra (Fig. 1d) could be fitted into three peaks at 529.3 eV, 530.7 eV, and 531.8 eV, which can be assigned to oxides, oxygen vacancies, and hydroxyl groups, respectively²⁹. The existence of oxygen vacancies is further evidenced by a strong diagnostic luminescent peak centered at ca. 500 nm in the PL spectrum (Supplementary Fig. 6). These results confirm the formation of oxygen vacancies as well as the coexistence of oxides, vacancies, and hydroxyl groups in rh-In₂O_{3-x}(OH)_y, which play a key role in the formation of SFLP^{32–34}.

CO₂ hydrogenation performance. The catalytic properties of the as-obtained rh-In₂O_{3-x}(OH)_y nanocrystals toward CO₂ hydrogenation with and without solar irradiation were evaluated in a flow reactor at different temperatures, under atmospheric pressure with a mixed feed gas of CO₂ and H₂ (H₂: CO₂ = 3: 1) (Fig. 2a, b). To investigate the polymorph effect of indium oxide on CO₂ hydrogenation performance, the cubic In₂O_{3-x}(OH)_y nanocrystals (annealing at 300 °C and denoted as c-In₂O_{3-x}(OH)_y) with similar porous morphology and crystalline size (Supplementary Fig. 7) were synthesized based on previous studies²⁹ and utilized as a reference material for comparison. The catalytic performance of the selected photocatalysts was tested from 200 °C to 300 °C. Only the as-prepared rh-In₂O_{3-x}(OH)_y was found to be able to catalyze the reverse water gas shift (RWGS) reaction at 200 °C with a CO rate of 51 μmol g_{cat}⁻¹ h⁻¹ and 60 μmol g_{cat}⁻¹ h⁻¹ for dark and light conditions, respectively. When the reaction temperature was increased to 230 °C, the rh-In₂O_{3-x}(OH)_y showed an increased CO formation rate of 185 μmol g_{cat}⁻¹ h⁻¹ (in dark) and 201 μmol g_{cat}⁻¹ h⁻¹ (in light). Furthermore, at this specific temperature, only the rh-In₂O_{3-x}(OH)_y was found to be capable of synthesizing CH₃OH with a rate of 55 μmol g_{cat}⁻¹ h⁻¹ (in dark) and 76 μmol g_{cat}⁻¹ h⁻¹ (in light).

When the temperature was increased to 250 °C, the rh-In₂O_{3-x}(OH)_y exhibited a CH₃OH rate of 105 μmol g_{cat}⁻¹ h⁻¹ (in dark) and 126 μmol g_{cat}⁻¹ h⁻¹ (in light). Thereafter, increasing the reaction temperature to 270 °C resulted in a CH₃OH formation rate of 180 μmol g_{cat}⁻¹ h⁻¹ and 144 μmol g_{cat}⁻¹ h⁻¹ with and without light irradiation. Such a solar powered CH₃OH rate of 180 μmol g_{cat}⁻¹ h⁻¹ is a performance record^{35–38} and about two times higher than the best reported solar CH₃OH maker (c-In₂O_{3-x}(OH)_y nanorods)³⁰ and 3.5 times higher than

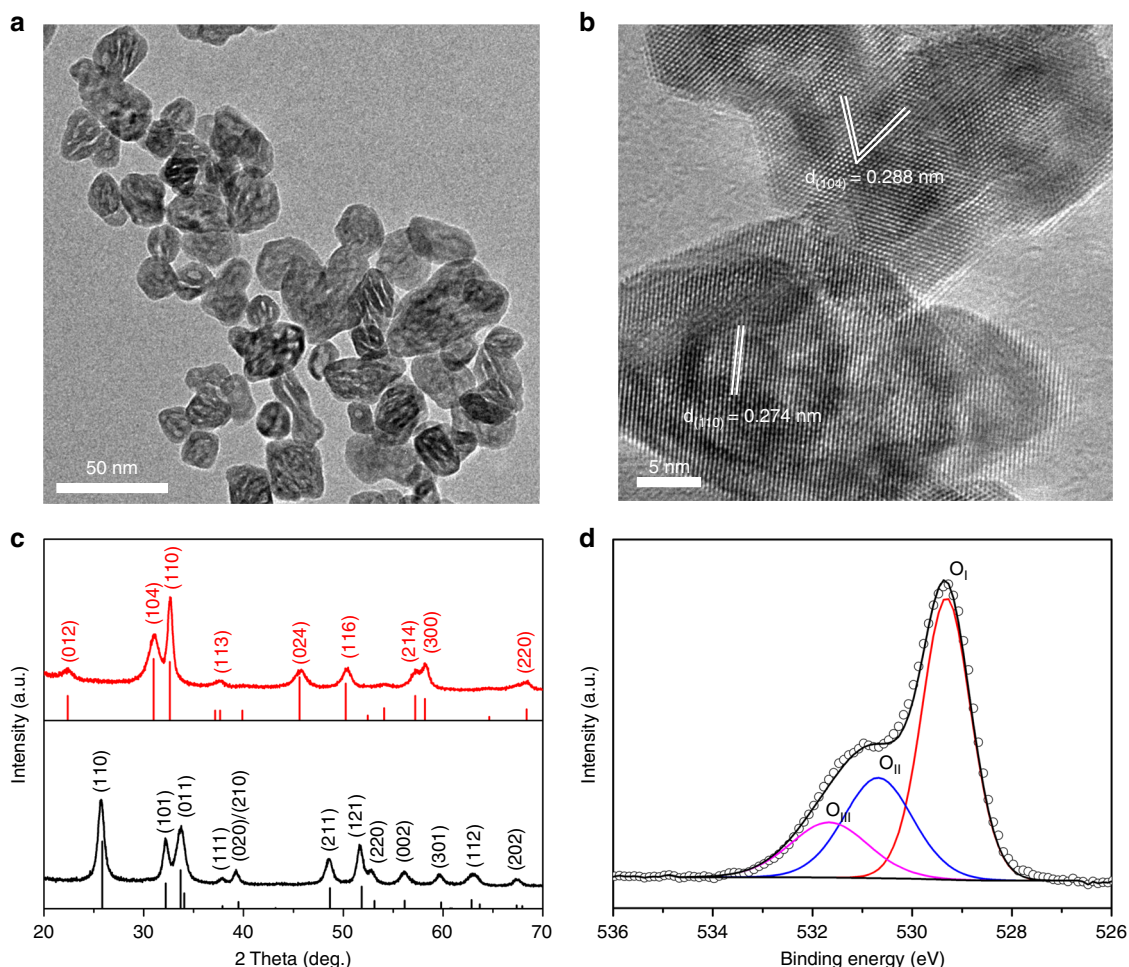


Fig. 1 Structural characterizations of InOOH precursor and rhombohedral $\text{In}_2\text{O}_{3-x}(\text{OH})_y$ nanocrystals. **a** TEM image of $\text{rh-In}_2\text{O}_{3-x}(\text{OH})_y$ nanocrystals. **b** HRTEM image of $\text{rh-In}_2\text{O}_{3-x}(\text{OH})_y$ nanocrystals. **c** PXRD patterns of InOOH precursor (black) and $\text{rh-In}_2\text{O}_{3-x}(\text{OH})_y$ nanocrystals (red). **d** High-resolution O 1s core level XPS spectra for $\text{rh-In}_2\text{O}_{3-x}(\text{OH})_y$ nanocrystals

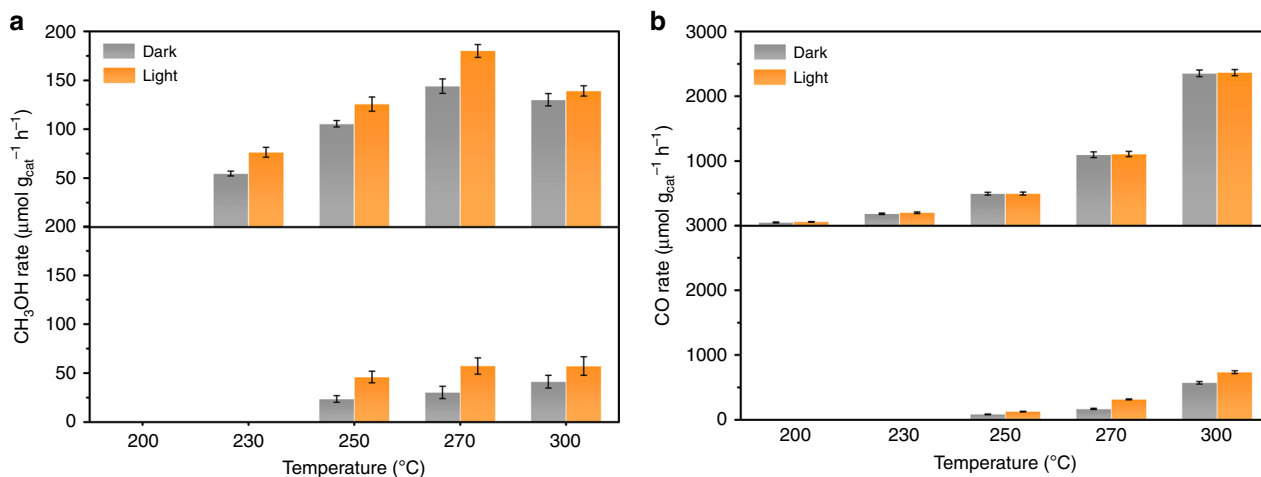


Fig. 2 Catalytic performance of $\text{rh-In}_2\text{O}_{3-x}(\text{OH})_y$ (up) and $\text{c-In}_2\text{O}_{3-x}(\text{OH})_y$ (down). **a** CH_3OH production rate at different reaction temperatures with and without solar irradiation. **b** CO production rate at different reaction temperatures with and without solar irradiation

the reference $\text{c-In}_2\text{O}_{3-x}(\text{OH})_y$ nanocrystals at similar reaction conditions. If catalytic performance is normalized on the basis of the specific surface area, the $\text{rh-In}_2\text{O}_{3-x}(\text{OH})_y$ would show a solar CH_3OH rate of $3.2 \mu\text{mol h}^{-1} \text{m}^{-2}$, which is ~ 5.8 times higher than that of $\text{c-In}_2\text{O}_{3-x}(\text{OH})_y$ nanorods, or 8.6 times higher than

that of $\text{c-In}_2\text{O}_{3-x}(\text{OH})_y$ nanocrystals. A control experiment shows that the CH_3OH selectivity of the commercial thermal catalyst (alumina supported copper zinc oxide) under the same photo-thermal reaction conditions and ambient pressure is $\sim 0.4\%$, which is 32 times lower than $\text{rh-In}_2\text{O}_{3-x}(\text{OH})_y$. Although the

CH₃OH productivity of rh-In₂O_{3-x}(OH)_y under high pressure needs further research, the rh-In₂O_{3-x}(OH)_y shows great potential for the future development of a solar fuels economy. Compared with traditional thermocatalytic technologies, solar-driven photocatalytic and photothermal catalytic CO₂ hydrogenation are proving to be promising strategies as they enable the utilization of abundant and clean solar energy, and during the catalytic process the photoexcitation of electrons into higher-energy states can lower the energy barrier of reaction³⁹.

Owing to the exothermic nature of the CH₃OH synthesis from H₂-CO₂, the CH₃OH rate at 300 °C decreases slightly to 139 μmol g_{cat}⁻¹ h⁻¹ (in light) and 130 μmol g_{cat}⁻¹ h⁻¹ (in dark). The enhancement of the CH₃OH rate with light irradiation can be attributed to the lower activation energy of the photocatalytic process as compared with the thermochemical process⁴⁰. The Arrhenius plots over rh-In₂O_{3-x}(OH)_y (Supplementary Fig. 8a) yield the apparent activation energy for CH₃OH production reaction, photocatalytically, at 38.4 kJ mol⁻¹, much smaller than 59.8 kJ mol⁻¹ for the thermochemical reaction. Moreover, the activation energy for CH₃OH production over rh-In₂O_{3-x}(OH)_y is much lower than that of c-In₂O_{3-x}(OH)_y under the same conditions (Supplementary Fig. 8b) and also lower than the reported value (103 kJ mol⁻¹) for cubic indium oxide under dark condition⁴¹.

To further support that CH₃OH production mainly proceeds through a photochemistry process, we also examined the dependence of CH₃OH rate on the wavelength of incident light. The results showed that the CH₃OH rate decreased with decreasing wavelength of the light (Supplementary Fig. 9), which matches well with the optical absorption spectra of rh-In₂O_{3-x}(OH)_y. The photo-enhancement for CH₃OH production almost disappeared when a 500 nm cutoff filter near the absorption edge was applied for the same light intensity.

Conversely, owing to the endothermic nature of the RWGS reaction, the CO rate is dramatically enhanced with increasing temperature and reaches about 2.4 mmol g_{cat}⁻¹ h⁻¹ at 300 °C. Such a CO formation rate is comparable to some of the most active noble metal decorated catalysts^{13,42} and ~3.2 times higher than that of the reference c-In₂O_{3-x}(OH)_y. Unlike CH₃OH performance, which can be enhanced by the light irradiation, CO performance was only enhanced by ~0.5 % under light irradiation (activation energy of ~84.8 kJ mol⁻¹ for both light and dark), which results in an enhanced solar CH₃OH selectivity (Supplementary Fig. 10). The distinct light-dependent trend reveals that the rate determining step for the production of CO appears to occur mainly by a thermochemical pathway in the electronic ground state, whereas the production of methanol has a contributing photochemical pathway involving electrons and holes in the electronic excited state thereby enhancing the activity of the SFLP. Moreover, to confirm the veracity of the CO and CH₃OH products from CO₂, isotope tracing experiments were conducted, where the ¹³CO₂ feedstock was utilized and the product gases were analyzed by gas chromatography–mass spectrometry (GC-MS), which confirmed the presence of ¹³CO and ¹³CH₃OH and the verity of the CO₂ derived products (Supplementary Fig. 11).

Tuning of SFLP toward CO₂ hydrogenation on rhombohedral In₂O_{3-x}(OH)_y. The structural parameters including concentration of oxygen vacancies and hydroxides are of great importance in forming the SFLP, and subsequently influence the photocatalytic performance. Accordingly, a series of rh-In₂O_{3-x}(OH)_y nanocrystals were synthesized from the InOOH precursor with different annealing temperatures of 250, 300, 350, and 400 °C, and denoted as rh-250, rh-300, rh-350, and rh-400, respectively.

PXRD patterns are found to be similar for samples annealed above 300 °C and could be assigned to the corundum structure type of In₂O₃ (Supplementary Fig. 12). Interestingly, the sample annealed at 250 °C exhibited a similar PXRD pattern to the InOOH precursor, which indicated a similar structure to InOOH, but with more oxygen vacancies and less hydroxide groups. The grain sizes for the prepared rh-In₂O_{3-x}(OH)_y nanocrystals showed a gradual decrease with elevated annealing temperatures, along with more nanopores generated during the dehydroxylation reaction (Supplementary Figs. 13 and 14). The specific surface areas of the rh-In₂O_{3-x}(OH)_y nanocrystals are slightly larger than the precursor InOOH, but are lower than the c-In₂O_{3-x}(OH)_y. All rh-In₂O_{3-x}(OH)_y samples show the same In(III) oxidation state, and the concentration of oxygen vacancies increases with increasing annealing temperatures, whereas the concentration of hydroxides decreases simultaneously (Supplementary Fig. 15). The band-edge absorption for all rh-In₂O_{3-x}(OH)_y nanocrystals and c-In₂O_{3-x}(OH)_y is located at ~450 nm, indicating similar electronic band structures (Supplementary Fig. 16).

The normalized catalytic activity for the various surface tuned rh-In₂O_{3-x}(OH)_y nanocrystals toward CO₂ hydrogenation, at 270 °C and 300 °C, with and without illumination, are shown in Fig. 3a, b, Supplementary Fig. 17 and summarized in Table 1. Although the rh-250 still showed similar PXRD patterns to InOOH, the thermal treatment was able to remove some lattice oxygen as well as hydroxide groups, which may result in the formation of SFLP and exhibit catalytic performance toward CO₂ hydrogenation. Other than the rh-250, the as-prepared rh-300, rh-350 and rh-400 exhibited diagnostic PXRD patterns, which can be assigned to the rhombohedral In₂O₃ structure with major exposed facets of (110) and (104) (Supplementary Fig. 18). The calculated grain size of rh-In₂O_{3-x}(OH)_y were ~11.5 ± 1.5 nm for all selected samples. All samples exhibited similar structural and morphological properties as well as photocatalytic performance, whereas the rh-350 showed the best catalytic performance.

The CO₂ adsorption properties were further investigated by CO₂-TPD experiments. As shown in Supplementary Fig. 19 and Table 1, the desorption temperature of CO₂ molecules on c-In₂O_{3-x}(OH)_y (~157 °C) is higher than that of all rhombohedral samples (~140 °C), indicating that the CO₂ molecules are more tightly adsorbed on the surface of c-In₂O_{3-x}(OH)_y. Moreover, the c-In₂O_{3-x}(OH)_y shows a larger peak area, reflecting an enhanced CO₂ adsorption. The reason for the higher CO₂ adsorption capacity of c-In₂O_{3-x}(OH)_y may simply be due to its larger surface area as compared with rhombohedral samples, so that the c-In₂O_{3-x}(OH)_y could provide a larger population of capture sites for CO₂. Even so, the enhanced CO₂ adsorption capacity of c-In₂O_{3-x}(OH)_y cannot contribute much to its photocatalytic CO₂ hydrogenation performance as the activity of rhombohedral samples greatly exceeded that of c-In₂O_{3-x}(OH)_y, and indicates the SFLP site served as the catalytically active site for CO₂ hydrogenation.

As SFLP can be considered as the active sites for the catalytic performance, the thermal treatment at 350 °C can efficiently remove lattice oxygen as well as hydroxide group to tune the surface into a ratio of 1:0.67 between oxygen vacancy and hydroxide group, which results in the optimal composition among all the samples tested. This can be further confirmed by the decreased activity of a H₂ treated rh-350 sample, which possessed relatively more oxygen vacancies and less hydroxide groups (Supplementary Fig. 20). Furthermore, as compared with CO, the production of methanol was significantly improved when irradiating with light, and exhibited an enhanced methanol selectivity as well.

Owing to its resulting best photocatalytic performance, the rh-350 was selected for further long-term stability testing at 270 °C

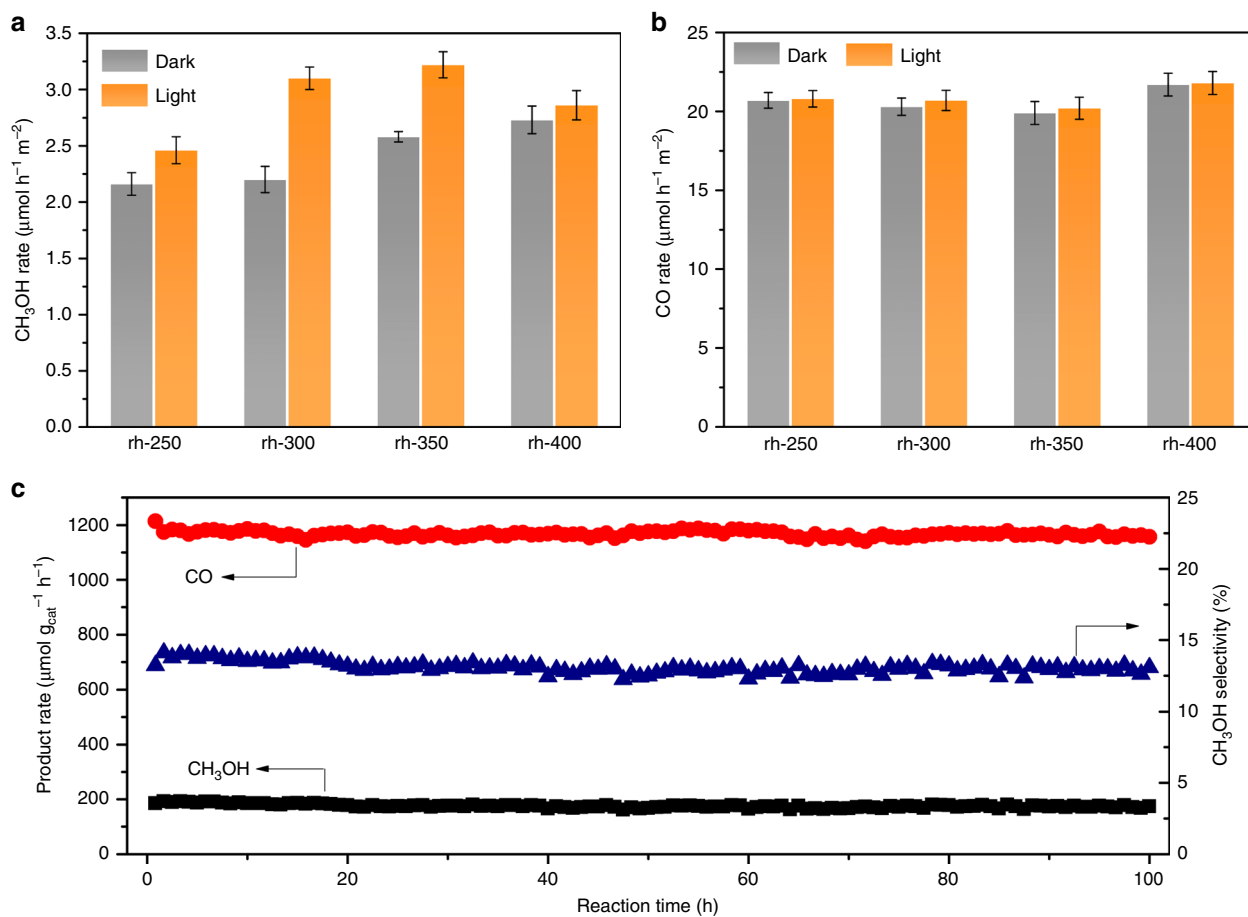


Fig. 3 Catalytic performance of various rh-In₂O_{3-x}(OH)_y nanocrystals. **a** Normalized CH₃OH production rate at 270 °C with and without light irradiation. **b** Normalized CO production rate at 270 °C with and without light irradiation. **c** Long-term (100 h) catalytic stability of rh-In₂O_{3-x}(OH)_y nanocrystals (rh-350) in catalyzing hydrogenation of CO₂ with light irradiation; reaction condition: 270 °C, 6 ml min⁻¹ H₂ and 2 ml min⁻¹ CO₂

Table 1 Summary of properties of various In₂O_{3-x}(OH)_y samples

Sample	D ^a	A ^b	E _g ^c	O _v ^d	OH ^e	R _{CO} ^f	R _{Methanol} ^g
rh-250	13	44	3.15	20.01	31.87	55.57	2.47
rh-300	13	54	3.01	21.35	20.64	44.87	3.10
rh-350	11	56	2.89	26.88	17.96	42.14	3.21
rh-400	10	51	2.88	30.00	16.40	38.31	2.86
c-In ₂ O _{3-x} (OH) _y	9.5	138	2.89	23.37	19.09	5.31	0.37

^aGrain size calculated from PXRD patterns (nm)

^bSpecific surface area obtained from BET measurement (m² g⁻¹)

^cBand gap energy (eV) calculated by fitting the reflectance spectra using K-M theory

^dConcentration of oxygen vacancies calculated from XPS (at. %)

^eConcentration of hydroxide groups calculated from XPS (at. %)

^fNormalized CO rate with solar irradiation obtained at 300 °C (μmol h⁻¹ m⁻²)

^gNormalized CH₃OH rate with solar irradiation obtained at 270 °C (μmol h⁻¹ m⁻²)

under atmospheric pressure with light irradiation. As shown in Fig. 3c, excellent stability resulted, with no significant change in production rate as well as selectivity in rh-350 over more than 100 h of continuous testing. As a result, methanol selectivity was maintained at 13% throughout the test, with the methanol rate of 170 μmol g_{cat}⁻¹ h⁻¹ and CO rate of 1150 μmol g_{cat}⁻¹ h⁻¹. Moreover, the used catalyst was also evaluated by XPS, PXRD, TEM, and no obvious oxidation state and structural changes were observed (Supplementary Figs. 21–23).

The SFLP on rhombohedral In₂O_{3-x}(OH)_y. The surface vacancy breaks the stable Lewis acid–base adjuncts (bridging In–O or In–OH), which can then create novel surface Lewis acidic sites, and the nearby surface hydroxide groups can function as the Lewis basic sites. As such, the strong charge difference between the resulting unsaturated In atom and the hydroxide group can form the SFLP on the single component metal oxide, which could further activate the small H₂ molecules. The determination of the presence of this SFLP on defect laden rh-In₂O_{3-x}(OH)_y was performed as follows.

Density functional theory (DFT) simulations were carried out to investigate the properties of the rhombohedral In₂O₃ nanocrystal. Based on PXRD patterns and HRTEM images, both of the major facets, (110) and (104), were used for the determination of the removal of lattice oxygen and addition of OH (as hydroxide). The (110) facet has been chosen for further calculation and explanation owing to the much stronger Bader charge of the present SFLP. To investigate this further, the bulk rhombohedral In₂O₃ structure was cut along the direction of (110) and generated the corresponding surface. As shown in Supplementary Fig. 24, possible vacancy sites were determined on the (110) rhombohedral In₂O₃ surface, and the formation energies of vacancies were calculated by using a known approach from the literature^{40,43}. All atomic removal steps were found to be endothermic in which the adsorption energy would range from 4.15 (for site 1) to 4.94 eV (for site 3) (Supplementary Table 2). To simulate the rh-In₂O_{3-x}(OH)_y surfaces, which contain the OH

group, the defected (110) rhombohedral $\text{In}_2\text{O}_{3-x}$ surface was used, which has the vacancies at site 1 and site 3 as the most and least favorable adsorption sites. Then the OH group was added to the defected surface at vacancy sites to form $\text{In}_2\text{O}_{3-x}(\text{OH})_y$, and the adsorption energy and charge transfer of binding were calculated (Supplementary Fig. 25). The amounts of total free energy change due to the binding of OH at site 1 and 3 of the defected surface are -3.97 eV and -4.30 eV, respectively, which indicate that the formation of hydroxylated nanostructures can be highly exothermic. Previous studies for the (111) surface of the $c\text{-In}_2\text{O}_{3-x}(\text{OH})_y$ nanostructure suggest that the O atom from the OH group and the near In atom (including $+1.66$ e and -1.50 e, respectively) can form an SFLP owing to the large charge difference⁴⁰. Thus, Bader charge calculations were performed to probe the localized charges on surface constituents, showing that the related O and In pair involve atomic local charges of $+2.90$ e and -2.09 e, and $+2.90$ e and -2.03 e, for site 1 and site 3 of the $\text{rh-In}_2\text{O}_{3-x}(\text{OH})_y$ nanostructure (Fig. 4a), respectively. The larger Bader charge between the Lewis acid and Lewis base on $\text{rh-In}_2\text{O}_{3-x}(\text{OH})_y$ could be caused by the following contributing effects. (i) A larger geometrical distance between the active O atom and In atom (3.65 Å) than that of the $c\text{-In}_2\text{O}_{3-x}(\text{OH})_y$ (3.20 Å), and (ii) a higher coordination number of the active In atom (6 in (110) facets) in $\text{rh-In}_2\text{O}_{3-x}(\text{OH})_y$ than that in $c\text{-In}_2\text{O}_{3-x}(\text{OH})_y$ (4 in (111) facets). Similar to the (110) facets, the SFLP can also be constructed by removing surface oxygen atom and introducing a hydroxide group on (104) facets of rhombohedral In_2O_3 (Supplementary Figs. 26 and 27). It reveals that the Lewis acidic In and Lewis basic O of the OH sites at the (104) surface possess Bader charges of $+1.61$ e and -1.12 e, respectively. In this scenario, the distance between Lewis acid and base is 3.75 Å.

The larger charge difference between the Lewis acid and Lewis base pairs in the (110) $\text{rh-In}_2\text{O}_{3-x}(\text{OH})_y$ structure compared with that of the (111) $c\text{-In}_2\text{O}_{3-x}(\text{OH})_y$ surface, envisages the $\text{rh-In}_2\text{O}_{3-x}(\text{OH})_y$ nanostructure would form more active Lewis acid–base pairs than the $c\text{-In}_2\text{O}_{3-x}(\text{OH})_y$ pair can muster, and therefore could strongly polarize H–H bonds and dissociate H_2 molecules. This prediction can be evidenced by the optimized configuration of hydrogenated $\text{rh-In}_2\text{O}_{3-x}(\text{OH})_y$, in which the H–H distance of H_2 is enlarged from 0.75 Å to 1.24 Å and the bond length of newly formed In–H and H–OH bonds are 1.86 and 1.07 Å, respectively (Supplementary Fig. 28). Furthermore, the relative activation energy barrier for H_2 heterolysis over $\text{rh-In}_2\text{O}_{3-x}(\text{OH})_y$ further confirms that the strong SFLP could enable more efficient H_2 dissociation. The calculation of reaction pathway and energy barrier of H_2 dissociation shows that H_2 dissociation on (110) $\text{rh-In}_2\text{O}_{3-x}(\text{OH})_y$ surface is endothermic with an activation energy barrier of 0.45 eV (Fig. 4b), which is much smaller than that (0.66 eV) on the (111) $c\text{-In}_2\text{O}_{3-x}(\text{OH})_y$ surface⁴⁰. More recently, experimental evidence for heterolysis of H_2 on the SFLP of $\text{rh-In}_2\text{O}_{3-x}(\text{OH})_y$ has also been observed by our group using a suite of five insightful spectroscopy probes including diffuse reflectance infrared Fourier-transform spectroscopy (DRIFTS), XPS, ^1H solid state MAS NMR, EPR, and UV-Vis-NIR, which provides an in-depth understanding of how gaseous H_2 interacts with nanostructured $\text{rh-In}_2\text{O}_{3-x}(\text{OH})_y$.

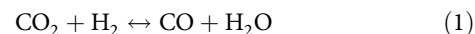
Investigation of the CO_2 hydrogenation pathway. In order to understand the catalytic pathway for CO_2 hydrogenation on $\text{rh-In}_2\text{O}_{3-x}(\text{OH})_y$ nanocrystals, in situ DRIFTS measurements were performed in a flow cell under reaction operando conditions. In the initial reaction stage, two primary surface species were observed, as shown in Fig. 5a. The first kind of species with fingerprint modes at 1505 , 1465 , and 1375 cm^{-1} can be assigned to chemisorbed CO_2 species including bicarbonate (HCO_3^-) and

carbonate (CO_3^{2-})^{44–47}. The second kind of species signaled by fingerprint modes at 1580 and 1360 cm^{-1} can be attributed to the asymmetric and symmetric OCO stretching vibrations of adsorbed bidentate formate (HCOO^*) species. This assignment is supported by two additional modes at 2870 cm^{-1} and 1390 cm^{-1} that are attributed to the stretching vibration $\nu(\text{CH})$ and bending vibration $\delta(\text{CH})$ of the same species^{48–50}. Along with the CO_2 hydrogenation the bicarbonate and carbonate species could readily be transformed to formate species, as evidenced by the decrease and disappearance of these bands. Apart from the formation of formate species, another important intermediate appears with diagnostic peaks at 2856 , 1448 , 1109 , and 1090 cm^{-1} in the spectra that are assigned to methoxy (H_3CO^*)^{48,49,51}. From these DRIFT results, CO_2 hydrogenation over $\text{rh-In}_2\text{O}_{3-x}(\text{OH})_y$ may proceed via formate intermediates (Supplementary Fig. 29, formate pathway), which eventually produces CH_3OH via the C–O bond cleavage and $^*\text{HCO}$ or $^*\text{H}_2\text{CO}$ intermediates^{48,52}. Simultaneously, we also observe the diagnostic vibrational modes of CO at bands 2227 and 2163 cm^{-1} , and water at 1649 cm^{-1} , indicative of another reaction pathway featuring a CO intermediate (Supplementary Fig. 29, RWGS pathway), which is produced from the RWGS reaction via carboxyl ($^*\text{HOCO}$) intermediates^{50,53}. However, such $^*\text{HOCO}$ intermediates are unstable and cannot be detected even at a low temperature (90 K)⁵⁴. To corroborate these experimental observations, free energy profiles for CO_2 hydrogenation via the proposed RWGS and formate pathways over $\text{rh-In}_2\text{O}_{3-x}(\text{OH})_y$ were calculated. The results suggest that via the RWGS pathway (Fig. 5b), except for product (CO, H_2O) desorption, the preceding hydrogenation reactions steps 1–3 are all exothermic. Similarly, steps 1–4 also behave in an exergonic nature via the formate pathway (Fig. 5c). These are different from the previously reported $c\text{-In}_2\text{O}_{3-x}(\text{OH})_y$ surface^{30,40}, resulting in the possibility of enhanced catalytic activity for hydrogenation of CO_2 . Notably, the smaller free energy barrier for the RWGS pathway is consistent with our experimental data of a faster CO production rate.

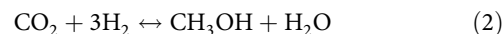
Discussion

As the first report that an SFLP in cubic $\text{In}_2\text{O}_{3-x}\text{OH}_y$ ⁴⁰, denoted $\text{InOH}\cdots\text{In}$, can facilitate heterolysis of H_2 to form $\text{InO-H}_2^+\cdots\text{InH}^-$, a number of chemical strategies have been devised to modify its Lewis acidity and Lewis basicity in order to tune its activity and selectivity in CO_2 (photo)catalysis.

To amplify, following heterolysis of H_2 on the SFLP, $\text{InO-H}\cdots\text{In} \rightarrow \text{InOH}_2^+\cdots\text{InH}^-$, the proton bound to the hydroxide Lewis base and hydride bound to the coordinately unsaturated indium can subsequently react with CO_2 to form CO in an endothermic reverse water gas shift reaction (Eq. 1):



and CH_3OH in an exothermic methanol forming reaction (Eq. 2):



in both cases with the desorption of co-product H_2O .

The rate and selectivity of these two reactions, which proceed simultaneously and by different pathways, facilitated by the SFLP, can be tailored advantageously by engineering the properties of the SFLP. In practice, this requires chemical means of adjusting the geometry of the SFLP and the negative and positive charge on the Lewis base and Lewis acid sites, respectively (Fig. 4a).

Note that these approaches to engineering the Lewis acidity and basicity of the SFLP refer to the electronic ground state of $\text{In}_2\text{O}_{3-x}(\text{OH})_y$. In the photo-excited state of $\text{In}_2\text{O}_{3-x}(\text{OH})_y$, the In2 and In1OH sites of the $\text{InOH}\cdots\text{In}$ SFLP serve as traps for electrons and holes, respectively, making the proton and hydride of

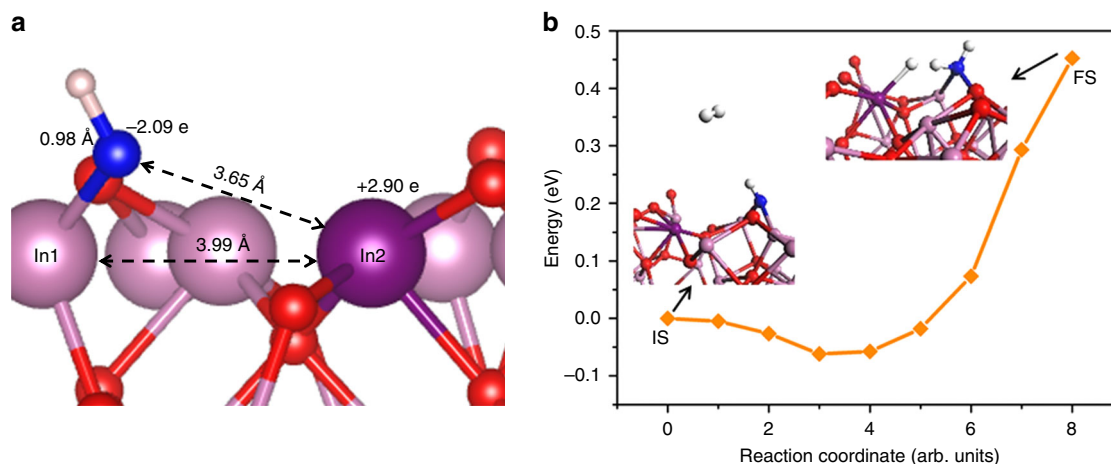


Fig. 4 Surface frustrated Lewis pairs on $\text{rh-In}_2\text{O}_{3-x}(\text{OH})_y$. **a** Side view of optimized configuration for (110) $\text{rh-In}_2\text{O}_{3-x}(\text{OH})_y$. **b** Reaction pathway and energy barrier of H_2 dissociation on (110) $\text{rh-In}_2\text{O}_{3-x}(\text{OH})_y$. White, pink, red, purple, and blue spheres represent H, In, O, Lewis pair In, and Lewis pair O atoms, respectively

the SFLP H_2 heterolysis intermediate $\text{InOH}_2^+\cdots\text{InH}^-$ more acidic and basic towards subsequent reactions with CO_2 ³². These traps also serve to lengthen the electron and hole excited state lifetimes, thereby enhancing the probability of reactions of $\text{InO-H}_2^+\cdots\text{InH}^-$ with CO_2 ^{33,34}. To this end, the charge-transfer dynamics of all samples were further investigated by time-resolved fluorescence spectroscopy (Supplementary Fig. 30). The curves can be fitted well using a triple exponential function (Supplementary Table 3 and Table 4). Following bandgap photoexcitation, electron-hole pairs relax into PL midgap SFLP defect sites, [O]/In(III) located closer in energy to the CB and OH similarly to the VB^{33,34}. This non-radiative process into SFLP sites, likely corresponds to the shortest ns lifetime τ_3 . The electron-hole pair residing in the SFLP can relax radiatively to yield the observed defect PL or non-radiatively to the electronic ground state as phonons or chemically reacting with reactants CO_2/H_2 (Supplementary Fig. 31). Notably, rh-350 with the longest average PL lifetime has the superior photocatalytic activity. This is another way of engineering the activity and selectivity of the SFLP. The solar advantage stems from the greater excited state Lewis acid and Lewis basicity of the SFLP of $\text{In}_2\text{O}_{3-x}(\text{OH})_y$, which is manifest experimentally in lower activation energies for the excited state pathway compared with the ground state.

Another point worth mentioning is the adsorption strength of intermediates and products to the SFLP, which can influence selectivity and conversion rates of the CO and CH_3OH pathways. For the case of a formate intermediate, created by the reaction of hydride with CO_2 , weak binding to the SFLP will favor the CO pathway (Supplementary Fig. 29, RWGS pathway), whereas strong binding will enable successive hydride transfers to formate, thereby favouring the CH_3OH pathway (Supplementary Fig. 29, formate pathway). In addition, the strongly adsorbing, surface coordinating products H_2O and CH_3OH , which have to be desorbed to make the CO_2 hydrogenation reactions catalytic, will act as rate limiting if the Lewis acidity of the In2 site is too high. Clearly, optimizing the rate and selectivity of CO_2 hydrogenation to CO and CH_3OH by $\text{In}_2\text{O}_{3-x}(\text{OH})_y$ requires a delicate balancing act of the Lewis acidity and Lewis basicity of the SFLP towards the binding of reactants, intermediates and products.

Approaches to SFLP engineering that have proven successful so far include control of oxygen vacancies and isomorphous substitution of the indium sites^{6,29}. In the case of [O]_v vacancies, the higher the substituting population is, the lower the oxygen

coordination number around the In(III) sites. This makes the In1OH more Lewis basic and the coordinately unsaturated In2 more Lewis acidic. For isomorphous substitution of In(III) by a similar-sized yet more electronegative element like Bi(III), exchange of the In2 site renders it more Lewis acidic, whereas replacement of In1 makes the hydroxide less Lewis basic.

Another strategy for tailoring the SFLP would be to change the distance between the Lewis acid and Lewis base sites (Fig. 4a), which would alter their charges and modify how they interact with H_2 . The geometry of the SFLP will vary between different crystal facets, which to implement will require strict control of the crystal morphology. Geometry changes of the SFLP are also achievable by polymorph engineering, a more straightforward method in practice, and the subject of the experimental and computational studies described herein.

In summary, we have demonstrated a polymorph selection strategy to modify the Lewis acidity and Lewis basicity of rhombohedral $\text{In}_2\text{O}_{3-x}(\text{OH})_y$ with a view to tuning activity and selectivity in gas-phase CO_2 (photo)catalysis. Significantly, $\text{rh-In}_2\text{O}_{3-x}(\text{OH})_y$ turns out to be a high performance photocatalyst, achieving champion CO_2 hydrogenation rates to CH_3OH and CO at atmospheric pressure. The superior catalytic performance appears to originate in the enhanced activity of surface Lewis acid–base pairs and strong propensity towards H_2 dissociation. An operando DRIFT study and DFT calculation provide information on the surface chemistry responsible for the formation of CH_3OH and CO, which appear to proceed by different reaction pathways. Based on the results and insight gained from this work, it should prove possible to optimize the Lewis acidity and Lewis basicity and enhance the photocatalytic performance of heterogeneous SFLP photocatalysts through polymorph selection. Furthermore, by understanding the distinct light-dependence of CO and CH_3OH formation and the impact of the electronic structure on CO_2 activation and H_2 dissociation by cubic and rhombohedral $\text{In}_2\text{O}_{3-x}(\text{OH})_y$, these heterogeneous SFLP systems can be incorporated into multi-component catalytic systems exemplified by polymorphic heterostructures, with distinct structures yet continuously adjustable fractions, enabling efficient CO_2 hydrogenation with front-line status.

Methods

Chemicals. All reagents used in the present study, including N,N -dimethylformamide (DMF), Indium(III) nitrate hydrate ($\text{In}(\text{NO}_3)_3 \cdot 4.5\text{H}_2\text{O}$, In 29%), and ethanol ($\text{C}_2\text{H}_5\text{OH}$) were analytical reagent grade and obtained from Sigma-

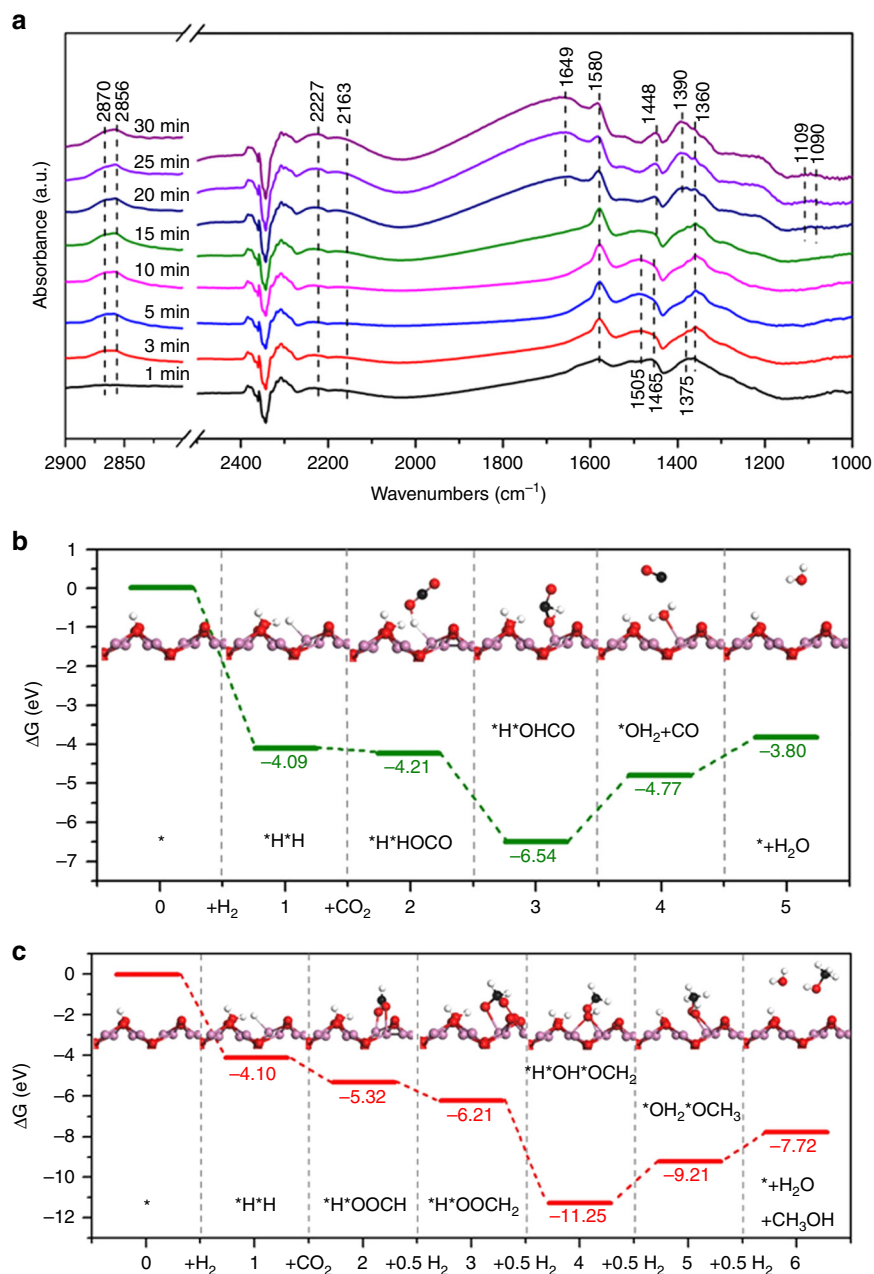


Fig. 5 CO₂ hydrogenation mechanism on rh-In₂O_{3-x}(OH)_y nanocrystals. **a** In situ DRIFTS spectra of surface species formed from CO₂ hydrogenation. **b** Energy profiles for CO₂ hydrogenation via the RWGS pathway. **c** Energy profiles for CO₂ hydrogenation via the formate pathway. Insets are the corresponding structures of reaction intermediates. The zero energy corresponds to the total free energy of the rh-In₂O_{3-x}(OH)_y nanocrystal

Aldrich. All chemicals were used as received. Deionized water was used throughout the synthesis.

Synthesis of InOOH precursor and rhombohedral In₂O_{3-x}(OH)_y nanocrystals.

In a typical synthesis of InOOH precursor, 0.3 g of In(NO₃)₃·4.5H₂O and 0.8 mL of distilled water were added to a 25 mL autoclave. DMF was then added to bring the total volume up to 17 mL. The aqueous solution was then heated at 150 °C for 24 h. After being cooled to room temperature, the white products were collected through centrifugation and washed with water and ethanol. The sample was finally dried at 60 °C. The dried InOOH precursors were then placed into an oven and treated at various temperatures (250–400 °C) in air for 4 h to obtain the final In₂O_{3-x}(OH)_y samples.

Characterization. PXRD was performed on a Bruker D2-Phaser X-ray diffractometer, using Cu Kα radiation at 30 kV. The HRTEM measurement was conducted using a JEM-2010 microscope working at 200 kV. Nitrogen Brunauer-Emmet-Teller (BET) adsorption isotherms were obtained using an

ASAP2020 M apparatus (Micromeritics Instrument Corp., USA). For BET surface area analyses, the samples were degassed in vacuum at 110 °C for 10 h and then measured at 77 K. The weight loss of InOOH precursor was carried out in a TA Instruments SDT Q600 thermogravimetric analyzer in an alumina pan under 100 mL min⁻¹ flow of compressed air. The temperature was steadily increased from room temperature (25 °C) to 580 °C at a rate of 5 °C min⁻¹. UV-visible diffuse reflectance spectra of the powders were obtained for the dry-pressed disk samples using a Cary 500 Scan Spectrophotometer (Varian, USA) over a range of 200–800 nm. BaSO₄ was used as a reflectance standard in the UV-visible diffuse reflectance experiment. XPS was performed using a PerkinElmer Phi 5500 ESCA spectrometer in an ultrahigh vacuum chamber with base pressure of 1 × 10⁻⁹ Torr. The spectrometer uses an Al Kα X-ray source operating at 15 kV and 27 A. The samples were coated onto carbon tape, and all results were calibrated to C1s 284.5 eV. The room temperature photoluminescence (PL) spectrum was measured on a FL/FS 920 (Edinburgh Instruments) equipped with a 450 W Xe arc lamp as the excitation source and a red sensitive Peltier element cooled Hamamatsu R2658 PMT as the detector. Time-resolved fluorescence decay spectra were recorded on the Delta Pro (HORIBA instruments) using a 357 nm laser as the excitation source. Carbon

dioxide temperature-programmed desorption (CO₂-TPD) measurements were performed on a Micromeritics AutoChem II 2920 chemisorption analyzer.

Gas-phase photocatalytic measurements. The gas-phase CO₂ hydrogenation experiments were conducted in an inner diameter of 2 mm tubular quartz reactor, in which ~20 mg of catalyst sample was packed into and fully irradiated with an unfiltered 130 W Xe lamp. The diameter of the light spot was ~2 cm, with an area of about 3.14 cm², which could fully cover the sample. An OMEGA temperature controller was attached to a heating cartridge inserted into the copper block along with a thermocouple inserted into the quartz tube in contact with the catalyst bed for control of the catalyst temperature. In a typical run, CO₂ or ¹³C isotope-labeled CO₂ (99 atom% ¹³C; Sigma) and H₂ with a ratio of 1: 3 (2 mL min⁻¹ and 6 mL min⁻¹) were introduced into the reactor by Alicat Scientific digital flow controllers. The amounts of CO and CH₃OH produced were analyzed by an on-line gas chromatograph (Agilent 7820 A), equipped with a thermal conductivity detector (TCD) and a flame ionization detector (FID).

In situ DRIFTS measurements. In situ DRIFTS measurements were performed to detect and characterize the possible surface intermediates over rhombohedral phase of In₂O_{3-x}(OH)_y nanocrystals under reaction conditions. The spectra were collected using a Fourier-transform infrared spectroscopy spectrometer (Thermo, Nicolet 6700) equipped with an MCT detector. Before measurement, the catalyst was purged with He at 350 °C for 2 h. The catalyst was subsequently cooled down to 230 °C. The background spectrum with a resolution of 4 cm⁻¹ was obtained at 230 °C in He flow. Then the catalyst was exposed to a CO₂/H₂/He mixture (1 mL min⁻¹ CO₂, 3 mL min⁻¹ H₂ and 16 mL min⁻¹ He) for 30 min. The in situ DRIFT spectra were recorded by collecting 32 scans at 4 cm⁻¹ resolution.

DFT calculations. Theoretical calculations are carried out with the context of DFT, as implemented in the Vienna ab initio simulation package. The exchange–correlation interactions were treated within the generalized gradient approximation in the form of the Perdew–Burke–Ernzerhof functional. The projector augmented wave approach with plane wave cutoff energy of 400 eV is used, and the convergence criteria are set to be 10⁻⁴ in energy and 0.02 eV Å⁻¹ in force. To model the rhombohedral In₂O₃ surfaces, four-layer slabs within vacuum spacing larger than 20 Å with the bottom two layers keep fixed are adopted. Brillouin zone integrations are performed over the Gamma point owing to the large supercell. Nudged elastic band method is used to determine the H₂ dissociation path and barrier.

Data availability

The data that support the plots within this paper and other findings of this study are available from the corresponding author upon reasonable request.

Received: 2 January 2019 Accepted: 16 May 2019

Published online: 07 June 2019

References

- Jia, J. et al. Heterogeneous catalytic hydrogenation of CO₂ by metal oxides: defect engineering-perfecting imperfection. *Chem. Soc. Rev.* **46**, 4631–4644 (2017).
- Zhao, Y. et al. Two-dimensional-related catalytic materials for solar-driven conversion of CO_x into valuable chemical feedstocks. *Chem. Soc. Rev.* **48**, 1972–2010 (2019).
- Manzoli, M. & Bonelli, B. Microwave, ultrasound, and mechanochemistry: unconventional tools that are used to obtain “smart” catalysts for CO₂ hydrogenation. *Catalysts* **8**, 262–296 (2018).
- Varghese, O. K. et al. High-rate solar photocatalytic conversion of CO₂ and water vapor to hydrocarbon fuels. *Nano. Lett.* **9**, 731–737 (2009).
- Gao, P. et al. Influence of Zr on the performance of Cu/Zn/Al/Zr catalysts via hydroxalate-like precursors for CO₂ hydrogenation to methanol. *J. Catal.* **298**, 51–60 (2013).
- Dong, Y. C. et al. Tailoring surface frustrated Lewis pairs of In₂O_{3-x}(OH)_y for gas-phase heterogeneous photocatalytic reduction of CO₂ by isomorphous substitution of In³⁺ with Bi³⁺. *Adv. Sci.* **5**, 1700732–1700742 (2018).
- Wang, J. J. et al. A highly selective and stable ZnO–ZrO₂ solid solution catalyst for CO₂ hydrogenation to methanol. *Sci. Adv.* **3**, 1701290–1701300 (2017).
- Liu, C. et al. Carbon dioxide conversion to methanol over size-selected Cu₄ clusters at low pressures. *J. Am. Chem. Soc.* **137**, 8676–8679 (2015).
- Lablokov, V. et al. Size-controlled model Co nanoparticle catalysts for CO₂ hydrogenation: synthesis, characterization, and catalytic reactions. *Nano. Lett.* **12**, 3091–3096 (2012).
- He, L. et al. Spatial separation of charge carriers in In₂O_{3-x}(OH)_y nanocrystal superstructures for enhanced gas-phase photocatalytic activity. *ACS Nano*. **10**, 5578–5586 (2016).
- Qu, J. et al. Shape effect of Pd-promoted Ga₂O₃ nanocatalysts for methanol synthesis by CO₂ hydrogenation. *J. Phys. Chem. C*. **118**, 24452–24466 (2014).
- Jia, J. et al. Visible and near-infrared photothermal catalyzed hydrogenation of gaseous CO₂ over nanostructured Pd@Nb₂O₅. *Adv. Sci.* **3**, 1600189–1600201 (2016).
- Jia, J. et al. Photothermal catalyst engineering: hydrogenation of gaseous CO₂ with high activity and tailored selectivity. *Adv. Sci.* **4**, 1700252–1700264 (2017).
- Hoch, L. B. et al. Nanostructured indium oxide coated silicon nanowire arrays: a hybrid photothermal/photochemical approach to solar fuels. *ACS Nano*. **10**, 9017–9025 (2016).
- Wu, H. C. et al. The effect of an Fe promoter on Cu/SiO₂ catalysts for improving their catalytic activity and stability in the water-gas shift reaction. *Catal. Sci. Technol.* **6**, 6087–6096 (2016).
- Wei, J. et al. Directly converting CO₂ into a gasoline fuel. *Nat. Commun.* **8**, 15174–15181 (2017).
- Martin, O. et al. Indium oxide as a superior catalyst for methanol synthesis by CO₂ hydrogenation. *Angew. Chem. Int. Ed.* **55**, 6261–6265 (2016).
- Tang, J. W. et al. Effects of substituting Sr²⁺ and Ba²⁺ for Ca²⁺ on the structural properties and photocatalytic behaviors of CaIn₂O₄. *Chem. Mater.* **16**, 1644–1649 (2004).
- Zou, Z. G. et al. Direct splitting of water under visible light irradiation with an oxide semiconductor photocatalyst. *Nature* **414**, 625–627 (2001).
- Tang, J. W. et al. Photophysical and photocatalytic properties of AgInW₂O₈. *J. Phys. Chem. B* **107**, 14265–14269 (2003).
- Hoch, L. B. et al. Effect of precursor selection on the photocatalytic performance of indium oxide nanomaterials for gas-phase CO₂ reduction. *Chem. Mater.* **28**, 4160–4168 (2016).
- He, Y. H. et al. A new application of nanocrystal In₂S₃ in efficient degradation of organic pollutants under visible light irradiation. *J. Phys. Chem. C*. **113**, 5254–5262 (2009).
- Lei, Z. B. et al. Photocatalytic water reduction under visible light on a novel ZnIn₂S₄ catalyst synthesized by hydrothermal method. *Chem. Commun.* **7**, 2142–2143 (2003).
- Yan, T. J. et al. Efficient photocatalytic degradation of volatile organic compounds by porous indium hydroxide nanocrystals. *Environ. Sci. Technol.* **44**, 1380–1385 (2010).
- Li, Z. H. et al. Wide band gap p-block metal oxyhydroxide InOOH: a new durable photocatalyst for benzene degradation. *J. Phys. Chem. C*. **111**, 18348–18352 (2007).
- Johnson, J. A. et al. Facile control of the charge density and photocatalytic activity of an anionic indium porphyrin framework via in situ metalation. *J. Am. Chem. Soc.* **136**, 15881–15884 (2014).
- Karazhanov, S. Zh. et al. Phase stability, electronic structure, and optical properties of indium oxide polytypes. *Phys. Rev. B* **76**, 075129–075141 (2007).
- Pan, Y. X. et al. Photocatalytic CO₂ reduction by carbon-coated indium-oxide nanobelts. *J. Am. Chem. Soc.* **139**, 4123–4129 (2017).
- Hoch, L. B. et al. The rational design of a single-component photocatalyst for gas-phase CO₂ reduction using both UV and visible light. *Adv. Sci.* **1**, 1400013–1400022 (2014).
- Wang, L. et al. Photocatalytic hydrogenation of carbon dioxide with high selectivity to methanol at atmospheric pressure. *Joule* **2**, 1369–1381 (2018).
- Yan, T. J. et al. Controlled preparation of In₂O₃, InOOH and In(OH)₃ via a one-pot aqueous solvothermal route. *New J. Chem.* **32**, 1843–1846 (2008).
- Ghuman, K. K. et al. Surface analogues of molecular frustrated Lewis pairs in heterogeneous CO₂ hydrogenation catalysis. *ACS Catal.* **6**, 5764–5770 (2016).
- Hoch, L. B. et al. Carrier dynamics and the role of surface defects: Designing a photocatalyst for gas-phase CO₂ reduction. *Proc. Natl. Acad. Sci. USA* **113**, E8011–E8020 (2016).
- Ghuman, K. K. et al. Photoexcited surface frustrated Lewis pairs for heterogeneous photocatalytic CO₂ reduction. *J. Am. Chem. Soc.* **138**, 1206–1214 (2016).
- Ahmed, N. et al. Photocatalytic conversion of carbon dioxide into methanol using zinc-copper-M(III) (M = aluminum, gallium) layered double hydroxides. *J. Catal.* **279**, 123–135 (2011).
- Ahmed, N. et al. Photocatalytic conversion of carbon dioxide into methanol using optimized layered double hydroxide catalysts. *Catal. Today* **185**, 263–269 (2012).
- Liang, L. et al. Single unit cell bismuth tungstate layers realizing robust solar CO₂ reduction to methanol. *Angew. Chem. Int. Ed.* **54**, 13971–13974 (2015).
- Li, H. et al. Carbon quantum dots/Cu₂O heterostructures for solar-light-driven conversion of CO₂ to methanol. *Adv. Energy Mater.* **5**, 1401077–1401082 (2015).
- Ghoussoub, M. et al. Principles of photothermal gas-phase heterogeneous CO₂ catalysis. *Energy Environ. Sci.* **12**, 1122–1142 (2019).

40. Ghuman, K. K. et al. Illuminating CO₂ reduction on frustrated Lewis pair surfaces: Investigating the role of surface hydroxides and oxygen vacancies on nanocrystalline In₂O_{3-x}(OH)_y. *Phys. Chem. Chem. Phys.* **17**, 14623–14635 (2015).
41. Frei, M. S. et al. Mechanism and microkinetics of methanol synthesis via CO₂ hydrogenation on indium oxide. *J. Catal.* **361**, 313–321 (2018).
42. Liu, H. et al. Conversion of carbon dioxide by methane reforming under visible-light irradiation: Surface-plasmon-mediated nonpolar molecule activation. *Angew. Chem. Int. Ed.* **54**, 11545–11549 (2015).
43. Walsh, A. Surface oxygen vacancy origin of electron accumulation in indium oxide. *Appl. Phys. Lett.* **98**, 261910–261912 (2011).
44. Tsuneoka, H. et al. Adsorbed species of CO₂ and H₂ on Ga₂O₃ for the photocatalytic reduction of CO₂. *J. Phys. Chem. C* **114**, 8892–8898 (2010).
45. Collins, S. E. et al. Infrared spectroscopic study of the carbon dioxide adsorption on the surface of Ga₂O₃ polymorphs. *J. Phys. Chem. B* **110**, 5498–5507 (2006).
46. Mino, L. et al. CO₂ capture by TiO₂ anatase surfaces: a combined DFT and FTIR study. *J. Phys. Chem. C* **118**, 25016–25026 (2014).
47. Wang, Y. et al. Selective photocatalytic CO₂ reduction to CH₄ over Pt/In₂O₃: Significant role of hydrogen adatom. *Appl. Catal. B Environ.* **226**, 544–553 (2018).
48. Kattel, S. et al. Optimizing binding energies of key intermediates for CO₂ hydrogenation to methanol over oxide-supported copper. *J. Am. Chem. Soc.* **138**, 12440–12450 (2016).
49. Bianchi, D. et al. Intermediate species on zirconia supported methanol aerogel catalysts. II. Adsorption of carbon monoxide on pure zirconia and on zirconia containing zinc oxide. *Appl. Catal. A Gen.* **105**, 223–249 (1993).
50. Wang, X. et al. Mechanism of CO₂ hydrogenation on Pd/Al₂O₃ catalysts: Kinetics and transient DRIFTS-MS studies. *ACS Catal.* **5**, 6337–6349 (2015).
51. Ouyang, F. et al. IR study on migration of ¹⁸OCH₃ species on ZrO₂. *Catal. Lett.* **50**, 179–181 (1998).
52. Liu, C. & Liu, P. Mechanistic study of methanol synthesis from CO₂ and H₂ on a modified model Mo₆S₈ cluster. *ACS Catal.* **5**, 1004–1012 (2015).
53. Schild, C. et al. On the mechanism of CO and CO₂ hydrogenation reactions on zirconia-supported catalysts: a diffuse reflectance FTIR study: Part II. Surface species on copper/zirconia catalysts: Implications for methanol synthesis selectivity. *J. Mol. Catal.* **63**, 243–254 (1990).
54. Senanayake, S. D. et al. Interaction of CO with OH on Au(111): HCOO, CO₃, and HOCO as key intermediates in the water-gas shift reaction. *J. Phys. Chem. C* **113**, 19536–19544 (2009).

Acknowledgements

T.Y. is thankful for financial support from the National Natural Science Foundation of China (21872081), Natural Science Foundation of Shandong Province (ZR2016BM04), China Postdoctoral Science Foundation (2015M572011, 2017T100494). B.H. and Y.Dai. acknowledge support from the Taishan Scholars Program of Shandong Province. G.A.O. acknowledges the financial support of the Ontario Ministry of Research and Innovation (MRI), the Ministry of Economic Development, Employment and Infrastructure

(MEDI), the Ministry of the Environment and Climate Change's (MOECC) Best in Science (BIS) Award, Ontario Center of Excellence Solutions 2030 Challenge Fund, Ministry of Research Innovation and Science (MRIS) Low Carbon Innovation Fund (LCIF), Imperial Oil, the University of Toronto's Connaught Innovation Fund (CIF), Connaught Global Challenge (CGC) Fund, and the Natural Sciences and Engineering Research Council of Canada (NSERC). Special thanks to Athan Tountas of the Chemical Engineering and Applied Chemistry and Keshav Raina of the Faculty of Forestry from University of Toronto for proofreading the manuscript.

Author contributions

T.Y. conducted the catalysts preparation and the catalysts testing flow experiments for CO₂ hydrogenation. L.W. performed the XPS characterization. Y.L., Y.Dai., B.H., and M. M. conducted and analyzed the DFT calculations. T.Y., L.W., and Y.Dong performed the in situ DRIFTS study. T.W. and F.M.A. performed the GC-MS test using ¹³CO₂ as well as the TEM characterization. T.Y., L.W., and G.A.O. conceived the project and co-wrote the manuscript. T.Y. and L.W. contributed equally to this work, and G.A.O. spearheaded the project. The manuscript was written through collective contributions from all authors. All authors approved the final version of the manuscript.

Additional information

Supplementary Information accompanies this paper at <https://doi.org/10.1038/s41467-019-10524-2>.

Competing interests: The authors declare no competing interests.

Reprints and permission information is available online at <http://npg.nature.com/reprintsandpermissions/>

Journal Peer Review Information: *Nature Communications* thanks the anonymous reviewer(s) for their contribution to the peer review of this work.

Publisher's note: Springer Nature remains neutral with regard to jurisdictional claims in published maps and institutional affiliations.



Open Access This article is licensed under a Creative Commons Attribution 4.0 International License, which permits use, sharing, adaptation, distribution and reproduction in any medium or format, as long as you give appropriate credit to the original author(s) and the source, provide a link to the Creative Commons license, and indicate if changes were made. The images or other third party material in this article are included in the article's Creative Commons license, unless indicated otherwise in a credit line to the material. If material is not included in the article's Creative Commons license and your intended use is not permitted by statutory regulation or exceeds the permitted use, you will need to obtain permission directly from the copyright holder. To view a copy of this license, visit <http://creativecommons.org/licenses/by/4.0/>.

© The Author(s) 2019